ENSO Bimodality and Extremes

Regina R. Rodrigues[1] (ID)**, Aneesh Subramanian[2]** (ID)**, Laure Zanna[3]** (ID)**, and Judith Berner[4]** (ID)

[1]Department of Oceanography, Federal University of Santa Catarina, Florianopolis, SC, Brazil, [2]Department of Atmospheric and Oceanic Sciences, University of Colorado Boulder, Boulder, CO, USA, [3]Department of Physics, University of Oxford, Oxford, UK, [4]National Center for Atmospheric Research, Boulder, CO, USA

Abstract Tropical sea surface temperature (SST) and winds vary on a wide range of timescales and have a substantial impact on weather and climate across the globe. Here we study the variability of SST and zonal wind during El Niño-Southern Oscillation (ENSO) between 1982 and 2014. We focus on changes in extreme statistics using higher-order moments of SST and zonal winds. We find that ENSO characteristics exhibit bimodal distributions and fat tails with extreme warm and cold temperatures in 1982–1999, but not during 2000–2014. The changes in the distributions coincide with changes in the intensity of ENSO events and the phase of the Interdecadal Pacific Oscillation. We also find that the strongest Easterly Wind Bursts occur during extreme El Niños and not during La Niñas. Maps of SST kurtosis can serve as a diagnostic for the thermocline feedback mechanism responsible for the differences in ENSO diversity between the two periods.

Plain Language Summary El Niño and La Niña in the Tropical Pacific Ocean affect weather, water resources, and fragile ecosystems around the globe. These phenomena have been extensively studied, yet we know relatively little on how and why El Niño and La Niña have changed over the past several decades. We use observational data sets of the ocean temperature and atmospheric winds to quantify and understand the nature of the change in these phenomena. We show that extreme El Niño and La Niña events occur more often in the 1980s and 1990s while in the past two decades there have been fewer extreme events in the Tropical Pacific. We also find that the strongest easterly wind anomalies occur during the extreme El Niño years only, which can then change how the atmosphere and ocean interact during these events compared to more moderate warm events. The Interdecadal Pacific Oscillation appears to modulate the decadal changes in the extremes of these events.

1. Introduction

The El Niño-Southern Oscillation (ENSO) phenomenon in the Tropical Pacific modulates global weather and climate on seasonal, interannual, and decadal timescales, having tremendous socioeconomic impacts (McPhaden et al., 2006). Therefore, understanding the mechanisms associated with ENSO and quantifying its variability are of great importance. ENSO is in part due to a positive feedback between the ocean and the atmosphere (Bjerknes, 1969). For an El Niño (warm) event, a weakening of the trade winds in the Tropical Pacific advects the warm pool water eastward and simultaneously triggers equatorial downwelling Kelvin waves, which will then deepen the thermocline in the eastern equatorial Pacific. As a result, the sea surface temperature (SST) in the eastern equatorial Pacific increases as the zonal SST gradient decreases, causing a further weakening of the trades (e.g., Battisti & Hirst, 1989; Harrison & Vecchi, 1997; Jin, 1997).

However, every ENSO event is different from each other (Timmermann et al., 2018). Chen, Lian, et al. (2015) put forward the existence of four distinct SST patterns associated with ENSO: three warm (El Niño) and one cold (La Niña). In addition, there is an asymmetry between warm and cold events; the strongest El Niños are larger than the largest La Niñas (Frauen & Dommenget, 2010; Levine et al., 2016). Two main ingredients determine the development and type of ENSO: high-frequency wind variability—namely, westerly and easterly wind bursts (WWBs and EWBs) in the western Tropical Pacific (Chiodi & Harrison, 2017; Harrison & Vecchi, 1997) and the buildup/halting of anomalous warm water volume in the upper Tropical Pacific (Meinen & McPhaden, 2000). While the latter has been associated with the basic ENSO cycle described earlier, the former is responsible for ENSO diversity and asymmetry. Chen, Lian, et al. (2015) show that it is possible to simulate the canonical El Niño/La Niña cycle without WWBs. When superposed to the main wind field, WWBs produce extreme eastern Pacific El Niño and weak warm-pool El Niño events through the combined effects of equatorial wave dynamics and surface warm-water advection. Because of

the unidirectional nature of this interaction, extreme La Niñas are not generated leading to the asymmetry between La Niña and El Niño events.

Recent studies have shown that the high-frequency wind variability is state dependent and various models with multiplicative noise forcing have been successful in simulating ENSO amplitude and spatial asymmetry (Berner et al., 2018; Chen, Lian, et al., 2015; Chen, Li, et al., 2015; Eisenman et al., 2005; Gebbie & Tziperman, 2009; Kapur & Zhang, 2012; Lopez & Kirtman, 2015; Perez et al., 2005). Levine et al. (2016) show that the ENSO state modifies the fetch and the wind speed of WWBs, but also the number of WWBs increases following a strong WWB. However, a series of strong EWBs, leading the WWBs and event peak, can contribute to the buildup of the heat content in the western Pacific (Chen & Majda, 2017; Hu & Fedorov, 2016).

Since the early 2000s, there has been a decrease in the amplitude and frequency of the ENSO cycle (Hu & Fedorov, 2016; McPhaden & Lee, 2011). This change has been attributed to the Interdecadal Pacific Oscillation (IPO) phase change from positive to negative in 1999–2000, rather than anthropogenic forcing (Okumura et al., 2017). A negative phase of the IPO is generally associated with a strengthening of the Pacific trade winds leading to a La Niña-like state with cooling of the Tropical Pacific (England et al., 2014). Combined with a steeper thermocline slope, the increase in the trade winds inhibits the eastward migration of the warm water along the equatorial Pacific, reducing the warm water volume variability and ENSO amplitude (Hu et al., 2013). Indeed, the variance of the NINO3 index (SST anomalies averaged within 90°–150°W and 5°N–5°S) has reduced from 0.83 for 1980–1999 to 0.59 for 2000–2010 (McPhaden, 2012). El Niño frequency increased while its amplitude decreased for the later period. It is not clear, however, if these shifts in the observed properties of ENSO are accompanied by changes in the high-frequency wind variability, which seems to be the cause of ENSO diversity and asymmetry.

The objective of this study is to analyze the statistics of daily SST and zonal wind for the two distinct periods 1982–1999 and 2000–2014. The transition from the first to the second period is associated with a reduction in strong ENSO events and also with a change in the phase of the IPO. In particular, we will focus on the higher moments of SST and zonal wind to study their changes in the context of some of the recent theories explaining ENSO diversity and asymmetry. Early studies have shown that higher-order moments for SST fields are nonzero (An & Jin, 2004; Burgers & Stephenson, 1999). The use of extended daily data (section 2) unveils a strong bimodality in El Niño SST linked to WWBs (section 3) and reversal of the trades in the precursor season. Moreover, we find evidence that the strongest EWBs occur during the extreme El Niño years and not in La Niña years. The discussion of the results and conclusion are drawn in section 4.

2. Data and Methods

In this study, we use the $1/4° \times 1/4°$ gridded daily SST data from Optimum Interpolation SST for the period 1982–2014 (Reynolds et al., 2007), and zonal component of the wind obtained from the European Centre for Medium-Range Weather Forecasts ERA-Interim reanalysis for the same period (Dee et al., 2011). For the latter, daily values are obtained by averaging the 6-hourly data. We also use the NCEP-DOE Reanalysis 2 daily zonal wind data provided by the NOAA/OAR/ESRL PSD (Kanamitsu et al., 2002).

The definition of ENSO years follows that of Trenberth (1997) with three categories: El Niño, La Niña, and neutral years. We quantify deviations from normal distributions for ENSO years by examining the higher moments of SST and zonal wind. Skewness, which determines the asymmetry of a distribution, is given by $\langle(x-\bar{x})^3\rangle/\sigma^3$, and kurtosis, which characterizes the tail of a distribution and the existence of extreme events, by $(\langle(x-\bar{x})^4\rangle/\sigma^4)-3$, where $\bar{x}$ is the mean and σ is the standard deviation (*std*) of a time series *x*.

Tung et al. (2019) show four widely used definitions for calculating the IPO index in observations. While they differ in some details, they all show a change of the IPO index from positive to negative between 1998 and 2000. Here we assume the transition to have taken place in 1999/2000 and examine the higher moments for two distinct periods 1982–1999 and 2000–2014, P1 and P2, respectively, as well as for the whole period (1982–2014). Note that we do not include data from 2015 onward because the IPO changes sign back to positive between 2013 and 2014 (Meehl et al., 2016). Therefore, the strong El Niño event in 2015/2016 is not included in the analysis, but statistics for this event are shown in Figures S8–S11, and they exhibit similar characteristics as in P1. Some of the results for P1 and P2 are presented as anomalies relative to the whole

period. We also show the results for two distinct seasons, the ENSO precursor season from September to November (SON) and ENSO mature season from December to January (DJF).

Histograms are obtained by binning the daily SST data every 0.2 °C and the zonal wind data every 1 m/s. We use the Kolmogorov-Smirnov test to check if the probability density function distributions are different between the two periods, P1 and P2, or between different ENSO categories in the same period. The statistical significance of the maps of skewness and kurtosis is evaluated using a Monte Carlo test, randomly selecting the same number of ENSO days from the climatological sample, taking into account the data autocorrelation timescale. This process is repeated 10,000 times, and grid points where the skewness (kurtosis) is in the most extreme 5% of the surrogate skewness (kurtosis) are considered significant.

In addition, to validate our observational study, we repeat our analysis on a 500-year climate model control simulation provided by the so-called "Large Ensemble" with the Community Earth System Model, version 1 (Kay et al., 2015), which contains several IPO cycles. Since the control simulation is forced with constant pre-industrial forcing, there is no climate change signal, and all variability is solely natural. The IPO-index for the climate simulations is calculated following Parker et al. (2007) by filtering global SST with an 11-year fourth-order Chebychev low-pass filter and performing an Empirical Orthogonal Function analysis. We use the first, rather than the second, principal component as IPO index, since there is no climate trend as in the observations.

The WWBs are defined according to Harrison and Vecchi (1997). The zonal wind at 850 hPa is averaged over 5°S–5°N for a longitude window of 100°E–100°W. We categorized an event as a WWB if the maximum speed is at least 7 m/s with an anomalous speed exceeding 2 m/s, for a minimum of 5 days. We categorized an event as an EWB if the maximum wind speed is above 3 *std* for a minimum of 5 days (Hu & Fedorov, 2016).

3. Results

3.1. ENSO-Related Statistics for 1982–2014

Skewness maps of daily SST for SON (Figure 1a) and DJF (Figure 1d) show positive (negative) values in areas where the mean SST tends to be cooler (warmer) for ENSO years. In SON, positive skewness dominates in the eastern part of the basin south of the equator, mainly in the cold tongue region. In addition, a weak negative skewness is present in the central part of the basin and in part of the warm pool region. These skewness signatures are similar to early findings by Burgers and Stephenson (1999). In DJF, there are two regions of positive skewness north and south of the equator toward the eastern Pacific, consistent with the southward migration of the mean isotherms (gray contours) associated with the establishment of austral summer.

The maps of kurtosis exhibit strong negative signals in central equatorial Pacific between 160°E and 140°W (Figures 1g and 1j for SON and DJF, respectively), though they are not statistically different from neutral years. In SON, the negative signal is flanked by positive kurtosis in the eastern and western Tropical Pacific. This result suggests the presence of heavy tails with extreme SST values in the cold tongue region. In DJF, the positive kurtosis south of the equator shifts westward, and, as a result, negative kurtosis is found along the South American coast. This westward shift of positive values from SON to DJF is also evident in the maps of skewness (Figures 1a and 1d) and is likely to be due to the westward shift of the SST pattern as the ENSO events develop further (Kug et al., 2009).

Figure 2 shows the distribution of daily SSTs in the NINO3 region for SON and DJF. The distributions for 1982–2014 during the peak-ENSO season (row IV) exhibit warmer temperatures than during its precursor season (row I), with broader histograms during DJF. The most prominent feature in DJF (panel IV-d), and to some extent in SON (panel I-d), is the bimodal structure of the distributions, which is predominantly determined by the extreme warm temperatures associated with El Niño events (panels IV-b and I-b). Specifically, the distributions are not unimodal, showing two distinct peaks. This strong bimodality in warm events is likely related to amplifying feedbacks in the central and eastern Pacific (Capotondi, 2013; Marathe et al., 2015). While the extreme warm events stand out in the distributions (panels I-d and IV-d), extreme cold events only appear as a long tail rather than a distinct regime (panels I-a and IV-a).

Asymmetry in the distribution of zonal wind values for ENSO years is shown in Figures 3a and 3d for SON and DJF, respectively. Positive skewness is found where the zonal wind is negative and vice versa (e.g., Monahan, 2004). A region of strong positive skewness is found between 170°E and 150°W along the
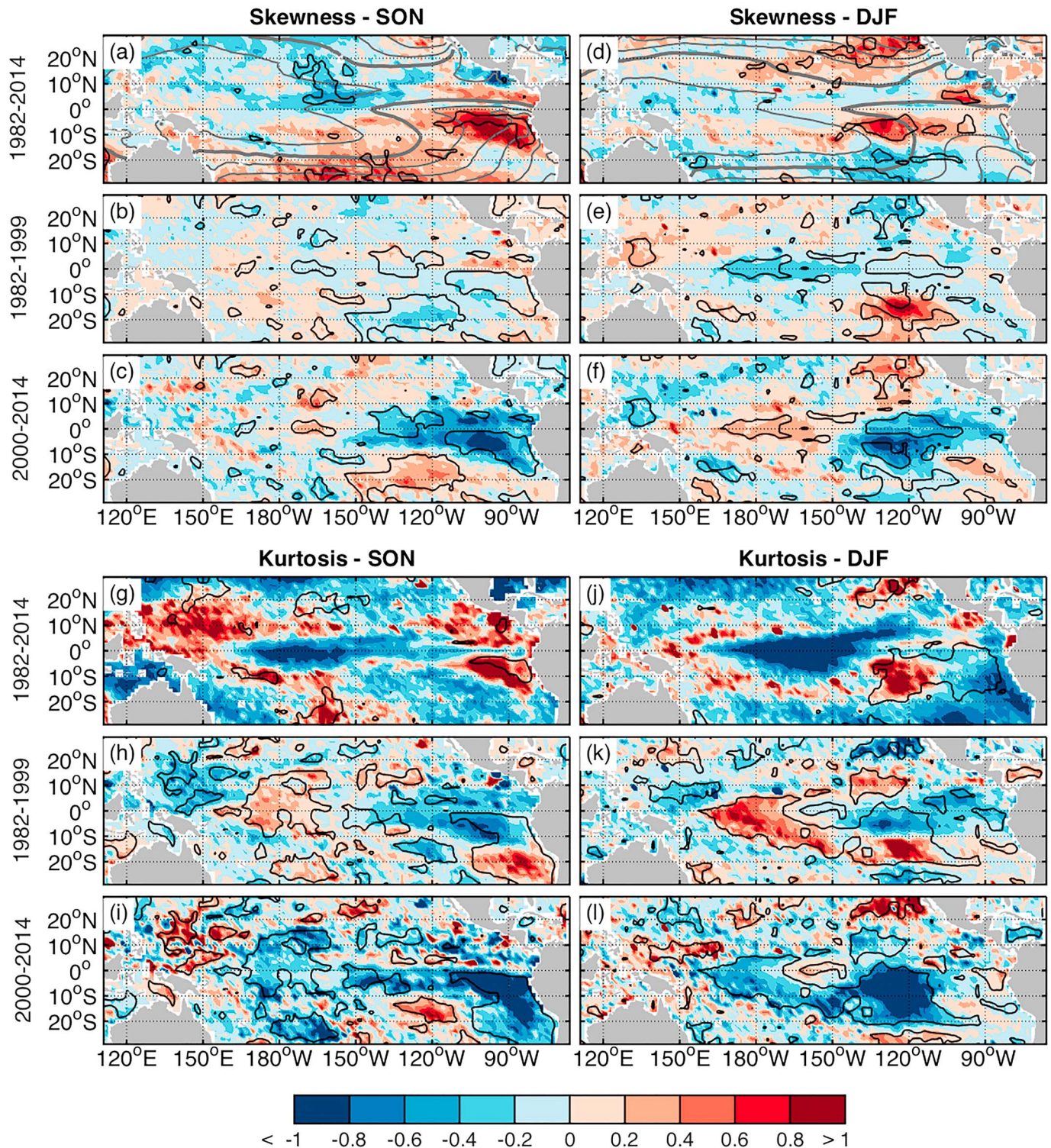
Figure 1. (a) Skewness of daily sea surface temperature for September to November (SON) during El Niño-Southern Oscillation years for the period of 1982–2014. Skewness anomalies for the periods (b) 1982–1999 and (c) 2000–2014; anomalies are defined with respect to the period of 1982–2014. Panels (d)–(f) are the same as (a)–(c), except for December to January (DJF). Gray contours in panels (a) and (d) are mean isotherms plotted every 2 °C; bold contour represents the 26°C isotherm. Black contours in panels (a) and (d) encompass areas where skewness for El Niño-Southern Oscillation years is statistically significantly different from neutral years and in panels (b), (c), and (e), (f) where the differences between P1 and P2 are statistically significant. Panels (g)–(l) are the same as (a)–(f), except for standardized kurtosis (−3).
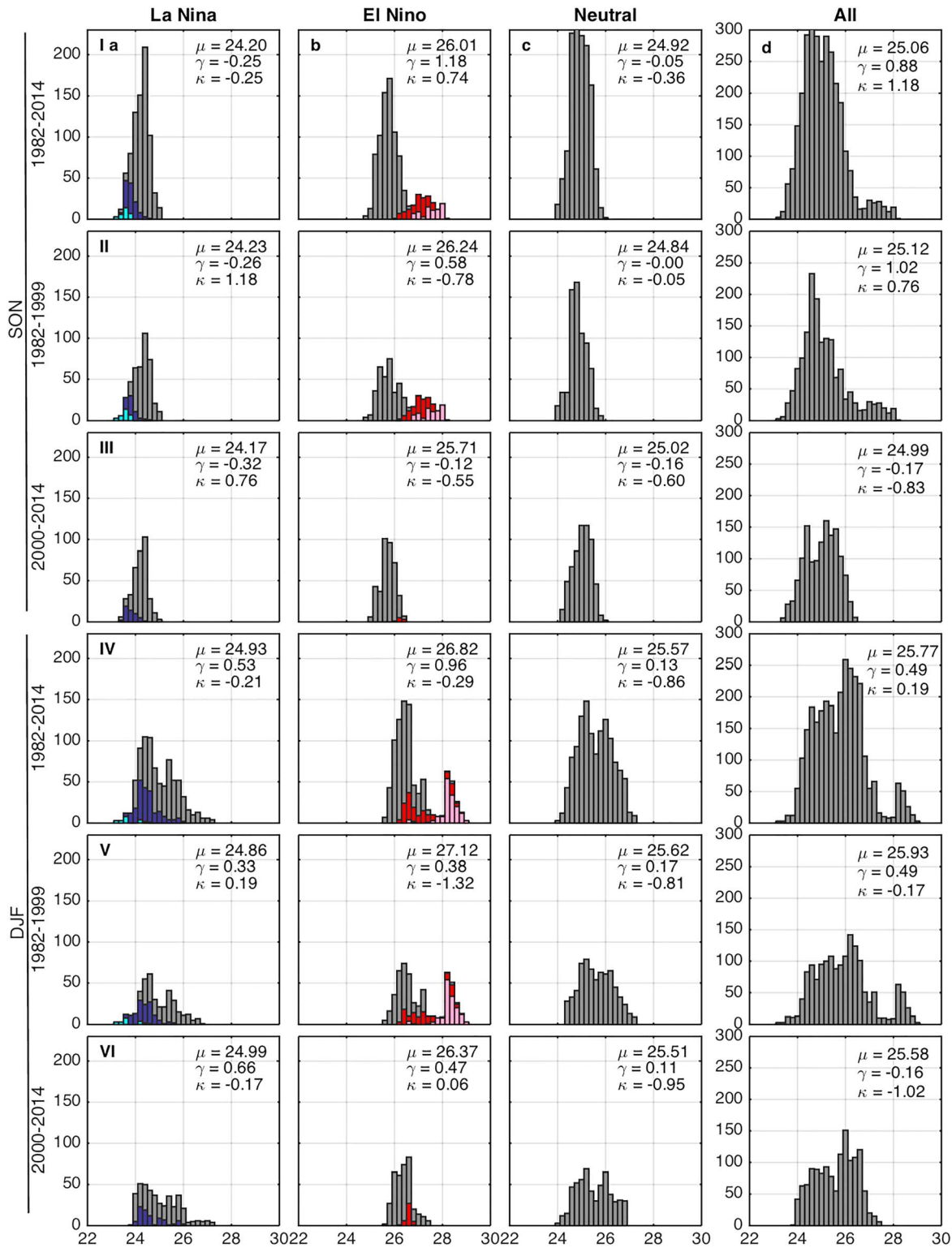
Figure 2. Distribution of the daily sea surface temperature (SST) averaged over the NINO3 region (5°N–5°S, 150°W–90°W) for September to November (rows I–III) and December to January (rows IV–VI) with *x* axis denoting SST values and *y* axis the number of occurrences: Row I corresponds to the whole period (1982–2014), row II to P1 (1982–1999), and row III for P2 (2000–2014). Rows I–III are the same as rows IV–VI, except for December to January. Columns (a)–(d) show SST distribution during La Niña years, El Niño years, neutral years, and all years, respectively. Extreme events are colored as follows: Dark blue corresponds to extreme La Niña events with SST anomalies below −1.5 °C and light blue below −2.0 °C, and dark red corresponds to extreme El Niño events with SST anomalies above +1.5 °C and pink above +2.0 °C. Mean (μ), skewness (γ), and kurtosis (χ) are shown in the top right of each panel.
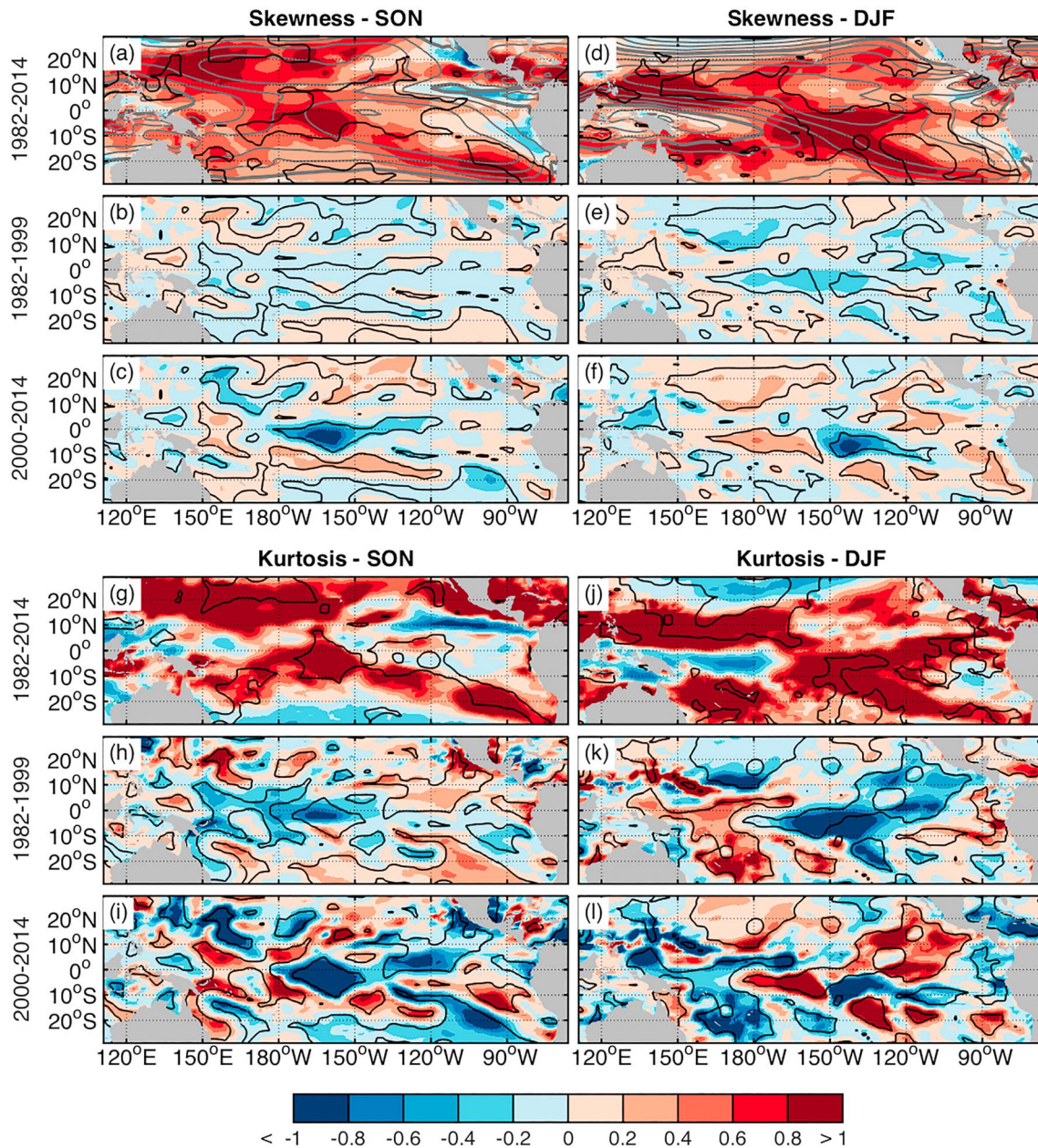
Figure 3. The same as Figure 1, except for skewness of daily zonal wind. Gray contours in panels (a) and (d) are mean isotachs plotted every 2 m/s. Bold contour represents 0 m/s isotach. Panels (g)–(l) are the same as panels (a)–(f) except for kurtosis of daily zonal wind.

equator in SON. This positive signal in skewness migrates to the east in DJF consistent with the eastward shift of the warm pool and weakening of the zonal SST gradient in this season, also evident in Figures 3g and 3j. Both skewness and kurtosis exhibit strong signal off the equator as well.

Figure 4 shows the distribution of daily zonal wind between 170°E and 120°W for SON and DJF. As for SSTs, the distributions for 1982–2014 during SON are more peaked than that during DJF. The effect of the weakening of the zonal SST gradient on the zonal wind, as part of the Bjerknes feedback, is evident by comparing the histograms for SON and DJF (rows I and IV). There is a decrease in the mean values from SON to DJF, accompanied by a decrease in positive skewness and kurtosis. The reduced strong gradients in SST will also result in less convection over the West Pacific and a shift of the wind distribution toward more negative values and less extremes. The zonal wind results described here are reproduced using NCEP-DOE Reanalysis (Figures S1 and S2).
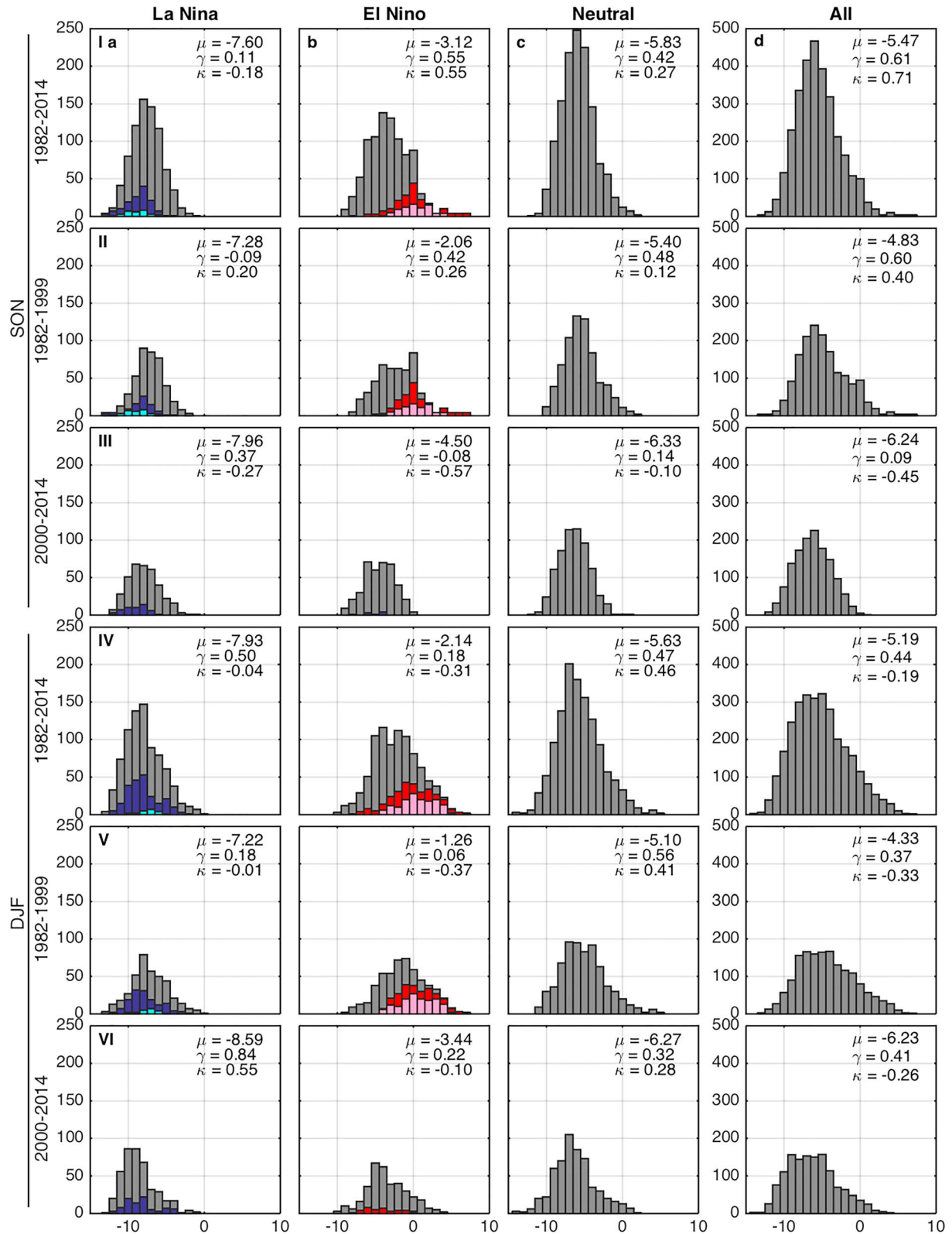
Figure 4. The same as Figure 2, except for daily zonal wind averaged over the warm pool region (5°N–5°S, 170°W–120°W).

3.2. Change Within the Two Subperiods

During the precursor (SON) and peak seasons (DJF), there is little change in skewness in P1 (1982–1999) compared to the full period studied (1982–2014; Figures 1b and 1e). The only exception is for a region of positive skewness anomaly between 10°S and 20°S centered at 120°W in DJF, which implies a stronger than average positive skewness. Repeating the analysis for same-length periods (1985–1999 and 2000–2014) does not change the results (Figure S3). In P2 (2000–2014), there are anomalous negative skewness signals in areas of positive skewness for the whole period, that is, in the eastern part of the basin along and south of the equator in SON (Figure 1c) and west of 120°W in DJF (Figure 1f). This is consistent with a decrease in extreme warm events in P2 compared to P1.

There is a reduction in kurtosis in P2 (negative anomalies) in the eastern Pacific in SON and in the central Pacific in DJF, mostly south of the equator. This is equivalent to less extreme events in P2 compared to both P1 and the entire period in those regions. During the ENSO season in P1, the kurtosis signal in the western Pacific is smaller than during the entire period while it increases in the central part. Therefore, we expect less extreme temperatures in the warm pool region with an increase in heavy tails in the central Pacific with more frequent eastern ENSO events. In P2, there is a westward extension of negative kurtosis due to less extreme events.

In histograms for SSTs in the NINO3 region (Figure 2), the strong bimodality in warm events is only present in P1 (see also Figure S4 for 1985–2014). Note that there is no sign of bimodality in SSTs in the NINO4 region (Figure S5). We see the distinct disappearance of all extreme warm events and a significant reduction in cold events in P2 (rows III and VI) compared to P1 (rows II and V). Therefore, P1 not only has more extreme warm El Niños but also has more extreme cold La Niñas compared to P2. This is corroborated by histograms for SSTs in the NINO4 region (Figure S5). Based on the Kolmogorov-Smirnov test, the distributions of SST in P1 are statistically different from those in P2, except for La Niña and neutral years in DJF (additional statistics are provided in Figure S6). To rule out the possibility that such differences could occur by chance, we have repeated the same analysis on a 500-year ensemble simulation, which spans several IPO cycles (see section 2). The model histograms are smoother compared to those of the observations, but present similar characteristics (Figure S7) such as El Niños are more frequent during periods of positive IPO whereas La Niñas during periods of negative IPO. Even though the model also shows that bimodality is due to extreme events (Figure S8), we cannot attribute the change to different phases of the IPO.

One could argue that the changes in the observed SST statistics between the two periods are due to intraevent variability, since we are using daily SST data. To check if they are rather due to interevent variability, we first plot the daily SST distribution for each El Niño event in SON and DJF (Figures S9 and S10, respectively). Although there is considerable intraevent variability (panels a–k), grouping events by type show that their distributions are practically Gaussian (panels l and m). When we group all El Niño events together (panel n), it is evident the bimodality is due to ENSO diversity. Note that here we include the strong El Niño event of 2015/2016. In addition, we present a scatterplot of daily values of NINO3 versus zonal wind averaged over the warm pool for neutral, La Niña, and El Niño events in SON and DJF (Figures S11 and S12, respectively). For both seasons, the daily SST values from the extreme events (oranges and reds) are practically separated from the rest, that is, weak-to-moderate El Niños (yellows), La Niñas (blues), and neutral years (grays). The model also shows that the extreme events are linked to the reversal of the wind in the Tropical Pacific (Figure S13). Finally, Figures S14 and S15 show the observed SST distributions applying respectively a high-pass filter (periods shorter than 90 days) and a low-pass filter (periods longer than 90 days) to the daily SST data (compare with Figure 2). The variability in the SST daily data is due to the low-frequency variability.

The zonal wind for P2 shows a strong anomalous negative skewness compared to that for the whole period (and P1) in central west Pacific during the precursor season (Figure 3). This is equivalent to less asymmetric distribution and a median closer to the mean. In the peak ENSO season, there is an anomalous dipole with negative anomalies in the central Pacific and positive anomalies in the eastern part in P2. This indicates a more symmetric distribution as the skewness is anomalously positive within the area of easterlies, and anomalously negative within the area of westerlies. Patterns of kurtosis are similar to those of skewness in SON, while in DJF P1 shows a clearly pronounced negative kurtosis anomaly in the central Pacific (Figure 3) shifted to the south, in agreement with previous study by Harrison and Vecchi (1997). As for

the SSTs, the maps indicate an overall decrease in extreme wind events during P2. (See also Figures S16 and S17 for 1985–2014.)

Based on the distributions of daily zonal wind for all categories during the precursor season, there are clearly more extremes in P1 than in P2 (positive vs. negative kurtosis, respectively, in rows II and III of Figure 4). As expected for warm events, there are more WWBs in P1 than in P2 (Figure S18). However, the extreme EWBs also occur during El Niños in P1, and not during La Niñas in P2, as one would expect. (See also Table S1 for the occurrence of WWBs and EWBs.) During DJF, the results are similar to the precursor season but perhaps less marked, especially for La Niñas, as the role of wind forcing is more important in SON than DJF. There are again more extreme EWBs in P1 compared to P2 (Figure S18 and Table S1), which agrees with our analysis of skewness and kurtosis (Figure 3). The distributions for all categories in both seasons in P1 are statistically different from those in P2 (Figure S19).

4. Discussion and Conclusions

We examined changes in ENSO variability in the Tropical Pacific, by quantitatively characterizing shifts in the statistics of SST and zonal wind. While previous studies have reported ENSO regime shifts based on either the second moment of SST or the Bjerknes stability index (Capotondi & Sardeshmukh, 2017; Hu et al., 2013; Lübbecke & McPhaden, 2014; McPhaden, 2012), we show the existence of strong contrast in higher-order moments' statistics between 1982–1999 (P1) and 2000–2014 (P2) for both winds and SST. In P1, for warm events, we see strong bimodality in SST in the NINO3 histogram, which is likely linked to nonlinear effects from the wind stress. In P1 extreme warm and cold events are present with asymmetric SST distribution. The decrease in the kurtosis of SST in the eastern Tropical Pacific in P2 is related to the lack of extreme ENSO events. Similar asymmetry is also present in the probability density function distributions of the wind field. Overall, we find that strongest EWBs occur during the extreme El Niño years in P1 and not in La Niña years in P2.

Our results show similar changes in the higher-order moments of winds and SST in the different periods supporting the hypothesis that there was a change in the feedbacks between the two periods studied here. Different feedbacks play prominent roles in the different flavors of ENSO events throughout the equatorial Pacific. According to the recharge oscillator framework (Jin, 1997), the feedbacks consist of two negative damping terms (thermal and mean advection) and three positive feedback terms (zonal advection, Ekman, and thermocline). Ekman feedback plays a negligible effect. Our results indicate that the changes seen in eastern and western Pacific could be due to changes in thermocline feedback (Hu et al., 2013) while the changes in the central Pacific are more likely due to changes in zonal advection feedback (Chen, Li, et al., 2015).

There is a decrease in the thermocline feedback in P2 because enhanced trade winds and steeper thermocline slope restrict the eastward migration of warm water from the western Pacific (Hu et al., 2013). Cooler SST anomalies in the east result in weaker convection during P2, shifting the ascending branch of the Walker cell to the west and confining the wind response to changes in the SST. Therefore, negative kurtosis anomalies in the central-western Pacific is an indication of a weaker thermocline feedback in P2, that is, a weaker SST-OLR relationship due to the presence of more widespread cold anomalies (less clouds) linked to a stronger mean east-west thermocline slope. So the SST kurtosis maps resembles those of regressed OLR onto SST anomalies (Figure 6 from Lübbecke & McPhaden, 2014) and can be used as a diagnostic for the SST-wind feedback mechanism. In addition, the westward shift of the positive skewness and kurtosis in SON for P2 is consistent with the more frequent occurrence of central Pacific El Niños with the zonal advection feedback being more important to establish the SST pattern (Kug et al., 2009).

The interaction between SST and WWBs has previously been shown to be an important contributor to adequate simulation and prediction of ENSO events (Gebbie et al., 2007). Previous studies show that models that represent state-dependent noise can represent the extreme El Niño statistic better than the models that do not have a state-dependent high-frequency variability in winds (Lopez & Kirtman, 2014, 2015; Takahashi & Dewitte, 2016). Our results show that the statistics of the zonal wind changes in response to the aforementioned ENSO feedbacks.

While there is no clear consensus on ENSO changes in future climate (Yeh et al., 2018), we can confidently suggest that multidecadal changes in extreme SST and wind have occurred in the past several decades, which might make detection of climate change in the Tropical Pacific more difficult. In P1, we notice that more extreme La Niñas are present and that those events coincide with a rebound of strong El Niños. There are not enough events to confidently validate this hypothesis. Meehl et al. (2016) suggest that the IPO has changed back to positive phase after 2013 and thus more extremes are expected with higher values of skewness and kurtosis just like in P1. Links between warm and cold events, and between higher-order moments and mean and standard deviation, require further work to understand how ENSO might change over the next several decades in the light of climate change.

References

An, S.-I., & Jin, F.-F. (2004). Nonlinearity and asymmetry of ENSO. *Journal of Climate*, *17*(12), 2399–2412. https://doi.org/10.1175/1520-0442(2004)017<2399:NAAOE>2.0.CO;2

Battisti, D. S., & Hirst, A. C. (1989). Interannual variability in a tropical atmosphere-ocean model: Influence of the basic state, ocean geometry and nonlinearity. *Journal of the Atmospheric Sciences*, *46*(12), 1687–1712. https://doi.org/10.1175/1520-0469(1989)046<1687:IVIATA>2.0.CO;2

Berner, J., Sardeshmukh, P. D., & Christensen, H. M. (2018). On the dynamical mechanisms governing El Niño-Southern Oscillation irregularity. *Journal of Climate*, *31*(20), 8401–8419. https://doi.org/10.1175/JCLI-D-18-0243.1

Bjerknes, J. (1969). Atmospheric teleconnections from the equatorial Pacific. *Monthly Weather Review*, *97*(3), 163–172. https://doi.org/10.1175/1520-0493(1969)097<0163:ATFTEP>2.3.CO;2

Burgers, G., & Stephenson, D. B. (1999). The "normality" of El Niño. *Geophysical Research Letters*, *26*(8), 1027–1030. https://doi.org/10.1029/1999GL900161

Capotondi, A. (2013). Enso diversity in the NCAR CCSM4 climate model. *Journal of Geophysical Research: Oceans*, *118*, 4755–4770. https://doi.org/10.1002/jgrc.20335

Capotondi, A., & Sardeshmukh, P. D. (2017). Is El Niño really changing? *Geophysical Research Letters*, *44*, 8548–8556. https://doi.org/10.1002/2017GL074515

Chen, D., Lian, T., Fu, C., Cane, M. A., Tang, Y., Murtugudde, R., et al. (2015). Strong influence of westerly wind bursts on El Niño diversity. *Nature Geoscience*, *8*(5), 339–345. https://doi.org/10.1038/ngeo2399

Chen, L., Li, T., & Yu, Y. (2015). Causes of strengthening and weakening of ENSO amplitude under global warming in four CMIP5 models. *Journal of Climate*, *28*(8), 3250–3274. https://doi.org/10.1175/JCLI-D-14-00439.1

Chen, N., & Majda, A. J. (2017). Simple stochastic dynamical models capturing the statistical diversity of El Niño Southern Oscillation. *Proceedings of the National Academy of Sciences*, *114*(7), 1468–1473. https://doi.org/10.1073/pnas.1620766114

Chiodi, A. M., & Harrison, D. (2017). Observed El Niño SST development and the effects of easterly and westerly wind events in 2014/15. *Journal of Climate*, *30*(4), 1505–1519. https://doi.org/10.1175/JCLI-D-16-0385.1

Dee, D. P., Uppala, S., Simmons, A., Berrisford, P., Poli, P., Kobayashi, S., et al. (2011). The ERA-Interim reanalysis: Configuration and performance of the data assimilation system. *Quarterly Journal of the Royal Meteorological Society*, *137*(656), 553–597. https://doi.org/10.1002/qj.828

Eisenman, I., Yu, L., & Tziperman, E. (2005). Westerly wind bursts: ENSO's tail rather than the dog? *Journal of Climate*, *18*(24), 5224–5238. https://doi.org/10.1175/JCLI3588.1

England, M. H., McGregor, S., Spence, P., Meehl, G. A., Timmermann, A., Cai, W., et al. (2014). Recent intensification of wind- driven circulation in the Pacific and the ongoing warming hiatus. *Nature Climate Change*, *4*(3), 222–227. https://doi.org/10.1038/nclimate2106

Frauen, C., & Dommenget, D. (2010). El Niño and La Niña amplitude asymmetry caused by atmospheric feedbacks. *Geophysical Research Letters*, *37*, L18801. https://doi.org/10.1029/2010GL044444

Gebbie, G., Eisenman, I., Wittenberg, A., & Tziperman, E. (2007). Modulation of westerly wind bursts by sea surface temperature: A semi-stochastic feedback for ENSO. *Journal of the Atmospheric Sciences*, *64*(9), 3281–3295. https://doi.org/10.1175/JAS4029.1

Gebbie, G., & Tziperman, E. (2009). Predictability of SST-modulated westerly wind bursts. *Journal of Climate*, *22*(14), 3894–3909. https://doi.org/10.1175/2009JCLI2516.1

Harrison, D., & Vecchi, G. A. (1997). Westerly wind events in the tropical Pacific. *Journal of Climate*, *10*(12), 3131–3156. https://doi.org/10.1175/1520-0442(1997)010<3131:WWEITT>2.0.CO;2

Hu, S., & Fedorov, A. V. (2016). Exceptionally strong easterly wind burst stalling El Niño of 2014. *Proceedings of the National Academy of Sciences*, *113*(8), 2005–2010. https://doi.org/10.1073/pnas.1514182113

Hu, Z.-Z., Kumar, A., Ren, H.-L., Wang, H., L'Heureux, M., & Jin, F.-F. (2013). Weakened interannual variability in the tropical Pacific Ocean since 2000. *Journal of Climate*, *26*(8), 2601–2613. https://doi.org/10.1175/JCLI-D-12-00265.1

Jin, F.-F. (1997). An equatorial ocean recharge paradigm for ENSO. Part I: Conceptual model. *Journal of the Atmospheric Sciences*, *54*(7), 811–829. https://doi.org/10.1175/1520-0469(1997)054<0811:AEORPF>2.0.CO;2

Kanamitsu, M., Ebisuzaki, W., Woollen, J., Yang, S. K., Hnilo, J. J., Fiorino, M., & Potter, G. L. (2002). NCEP–DOE AMIP-II Reanalysis (R-2). *Bulletin of the American Meteorological Society*, *83*(11), 1631–1644. https://doi.org/10.1175/BAMS-83-11-1631

Kapur, A., & Zhang, C. (2012). Multiplicative MJO forcing of ENSO. *Journal of Climate*, *25*(23), 8132–8147. https://doi.org/10.1175/JCLI-D-11-00609.1

Kay, J. E., Deser, C., Phillips, A., Mai, A., Hannay, C., Strand, G., et al. (2015). The Community Earth System Model (CESM) large ensemble project: A community resource for studying climate change in the presence of internal climate variability. *Bulletin of the American Meteorological Society*, *96*(8), 1333–1349. https://doi.org/10.1175/BAMS-D-13-00255.1

Kug, J. S., Jin, F. F., & An, S. I. (2009). Two types of El Niño events: Cold tongue El Niño and warm pool El Niño. *Journal of Climate*, *22*(6), 1499–1515. https://doi.org/10.1175/2008JCLI2624.1

Levine, A., Jin, F.-F., & McPhaden, M. J. (2016). Extreme noise-extreme El Niño: How state-dependent noise forcing creates El Niño-La Niña asymmetry. *Journal of Climate*, *29*(15), 5483–5499. https://doi.org/10.1175/JCLI-D-16-0091.1

Lopez, H., & Kirtman, B. P. (2014). WWBs, ENSO predictability, the spring barrier and extreme events. *Journal of Geophysical Research: Atmospheres*, *119*, 10,114–10,138. https://doi.org/10.1002/2014JD021908

Lopez, H., & Kirtman, B. P. (2015). Tropical Pacific internal atmospheric dynamics and resolution in a coupled GCM. *Climate Dynamics*, *44*(1-2), 509–527. https://doi.org/10.1007/s00382-014-2220-7

Lübbecke, J. F., & McPhaden, M. J. (2014). Assessing the twenty-first-century shift in ENSO variability in terms of the Bjerknes stability index. *Journal of Climate*, *27*(7), 2577–2587. https://doi.org/10.1175/JCLI-D-13-00438.1

Marathe, S., Ashok, K., Swapna, P., & Sabin, T. (2015). Revisiting El Niño Modoki. *Climate Dynamics*, *45*(11-12), 3527–3545. https://doi.org/10.1007/s00382-015-2555-8

McPhaden, M. J. (2012). A 21st century shift in the relationship between ENSO SST and warm water volume anomalies. *Geophysical Research Letters*, *39*, L09706. https://doi.org/10.1029/2012GL051826

McPhaden, M. J., & Lee, T. (2011). El Niño and its relationship to changing background conditions in the tropical Pacific Ocean. *Geophysical Research Letters*, *38*, L15709. https://doi.org/10.1029/2011GL048275

McPhaden, M. J., Zebiak, S. E., & Glantz, M. H. (2006). ENSO as an integrating concept in Earth Science. *Science*, *314*(5806), 1740–1745. https://doi.org/10.1126/science.1132588

Meehl, G. A., Hu, A., & Teng, H. (2016). Initialized decadal prediction for transition to positive phase of the Interdecadal Pacific Oscillation. *Nature Communications*, *7*(1), 11718. https://doi.org/10.1038/ncomms11718

Meinen, C. S., & McPhaden, M. J. (2000). Observations of warm water volume changes in the equatorial Pacific and their relationship to El Niño and La Niña. *Journal of Climate*, *13*(20), 3551–3559. https://doi.org/10.1175/1520-0442(2000)013<3551:OOWWVC>2.0.CO;2

Monahan, A. H. (2004). A simple model for the skewness of global sea surface winds. *Journal of the Atmospheric Sciences*, *61*(16), 2037–2049. https://doi.org/10.1175/1520-0469(2004)061<2037:ASMFTS>2.0.CO;2

Okumura, Y. M., Sun, T., & Wu, X. (2017). Asymmetric modulation of El Niño and La Niña and the linkage to tropical Pacific decadal variability. *Journal of Climate*, *30*(12), 4705–4733. https://doi.org/10.1175/JCLI-D-16-0680.1

Parker, D., Folland, C. K., Scaife, A. A., Knight, J., Colman, A. W., Baines, P., & Dong, B. (2007). Decadal and multidecadal variability in the climate change background. *Journal of Geophysical Research*, *112*(D18), 112. https://doi.org/10.1029/2007JD008411

Perez, C. L., Moore, A. M., Zavala-Garay, J., & Kleeman, R. (2005). A comparison of the influence of additive and multiplicative stochastic forcing on a coupled model of ENSO. *Journal of Climate*, *18*(23), 5066–5085. https://doi.org/10.1175/JCLI3596.1

Reynolds, R. W., Smith, T. M., Liu, C., Chelton, D. B., Casey, K. S., & Schlax, M. G. (2007). Daily high-resolution-blended analyses for sea surface temperature. *Journal of Climate*, *20*(22), 5473–5496. https://doi.org/10.1175/2007JCLI1824.1

Takahashi, K., & Dewitte, B. (2016). Strong and moderate nonlinear El Niño regimes. *Climate Dynamics*, *46*(5-6), 1627–1645. https://doi.org/10.1007/s00382-015-2665-3

Timmermann, A., An, S. I., Kug, J. S., Jin, F. F., Cai, W., Capotondi, A., et al. (2018). El Niño-Southern Oscillation complexity. *Nature*, *559*(7715), 535–545. https://doi.org/10.1038/s41586-018-0252-6

Trenberth, K. E. (1997). The definition of El Niño. *Bulletin of the American Meteorological Society*, *78*(12), 2771–2777. https://doi.org/10.1175/1520-0477(1997)078<2771:TDOENO>2.0.CO;2

Tung, K. K., Chen, X., Zhou, J., & Li, K. F. (2019). Interdecadal variability in pan-Pacific and global SST, revisited. *Climate Dynamics*, *52*(3-4), 2145–2157. https://doi.org/10.1007/s00382-018-4240-1

Yeh, S.-W., Cai, W., Min, S.-K., McPhaden, M. J., Dommenget, D., Dewitte, B., & Kug, J.-S. (2018). ENSO atmospheric teleconnections and their response to greenhouse gas forcing. *Reviews of Geophysics*, *56*(1), 185–206. https://doi.org/10.1002/2017RG000568